17. G. Paglia, E. S. Bozin, S. J. L. Billinge, *Chem. Mater.* **18**, 3242 (2006).
18. W. H. Casey, *Chem. Rev.* **106**, 1 (2006).
19. I. Joumard *et al.*, *Phys. Rev. B* **74**, 205411 (2006).
20. G. W. Brady *et al.*, *Biochemistry* **7**, 2185 (1968).
21. R. A. Eggleton, R. W. Fitzpatrick, *Clays Clay Miner.* **36**, 111 (1988).
22. Q. A. Pankhurst, R. J. Pollard, *Clays Clay Miner.* **40**, 268 (1992).
23. Y. Pan *et al.*, *Micron* **37**, 403 (2006).
24. Y. Pan, Ph.D. thesis, University of Leeds, Leeds, UK (2007).
25. Y. Guyodo *et al.*, *Physics of the Earth and Planetary Interiors* **154**, 222 (2006).
26. E. Murad, U. Schwertmann, *Am. Mineral.* **65**, 1044 (1980).
27. J. van Slageren *et al.*, *Phys. Rev. B* **73**, 014422 (2006).
28. P. Juhas, D. M. Cherba, P. M. Duxbury, W. F. Punch, S. J. L. Billinge, *Nature* **440**, 655 (2006).
29. V. Petkov *et al.*, *Phys. Rev. B* **65**, 092105 (2002).
30. B. Gilbert, F. Huang, H. Z. Zhang, G. A. Waychunas, J. F. Banfield, *Science* **305**, 651 (2004).
31. This work is dedicated in memoriam to Charles E. McClennen, Professor of Geology, Colgate University. Support provided by the Center for Environmental Molecular Science (CEMS); NSF Awards CHE0221934, DMR-045244, and EAR-0510501; the U.S. Department of Education through the Graduate Assistance in Areas of National Need Program Sponsor identification P200A060248; and the U.S. Department of Energy, Basic Energy Sciences grant no. DE-FG02-03ER-47085. Data collection was performed at X-Ray Operation and Research beamline 11-ID-B at the Advance Photon Source, Argonne National Laboratory, and use is supported by the U.S. Department of Energy, Office of Science, Office of Basic Energy Sciences, under contract no. DE-AC02-06CH11357. We thank D. Dyar for her efforts in the collection of Mössbauer data on these samples.

Supporting Online Material

www.sciencemag.org/cgi/content/full/1142525/DC1
SOM Text
Fig. S1
Tables S1 and S2
Crystallographic Information Files
References

14 March 2007; accepted 9 May 2007
Published online 24 May 2007;
10.1126/science.1142525
Include this information when citing this paper.

Deformation of $(Mg,Fe)SiO_3$ Post-Perovskite and D″ Anisotropy

Sébastien Merkel,[1,2]* Allen K. McNamara,[3] Atsushi Kubo,[4]† Sergio Speziale,[1]‡ Lowell Miyagi,[1] Yue Meng,[5] Thomas S. Duffy,[4] Hans-Rudolf Wenk[1]

Polycrystalline $(Mg_{0.9},Fe_{0.1})SiO_3$ post-perovskite was plastically deformed in the diamond anvil cell between 145 and 157 gigapascals. The lattice-preferred orientations obtained in the sample suggest that slip on planes near (100) and (110) dominate plastic deformation under these conditions. Assuming similar behavior at lower mantle conditions, we simulated plastic strains and the contribution of post-perovskite to anisotropy in the D″ region at the Earth core-mantle boundary using numerical convection and viscoplastic polycrystal plasticity models. We find a significant depth dependence of the anisotropy that only develops near and beyond the turning point of a downwelling slab. Our calculated anisotropies are strongly dependent on the choice of elastic moduli and remain hard to reconcile with seismic observations.

Seismological observations of the lowermost mantle (the D″ region) have revealed a region of great complexity distinct from the overlying deep mantle (*1*, *2*). Unlike the bulk of the lower mantle, the core-mantle boundary (CMB) includes large-scale regions with apparent seismic anisotropy (*3*). It has been suggested that this anisotropy could reflect lattice-preferred orientation (LPO) of minerals (*4*) or alignment of structural elements, including layers of melt (*5*, *6*). A number of lines of evidence now suggest that the transition from a perovskite (Pv) to a post-perovskite (pPv) phase in $(Mg,Fe)SiO_3$ (*7*, *8*) could explain important properties of D″ (*9*–*13*). However, the influence of this phase transition on our understanding of D″ anisotropy remains ambiguous. In this paper, we present multiscale modeling of deformation-induced anisotropy from $(Mg,Fe)SiO_3$-pPv in D″. This work is a combination of high-pressure deformation experiments on $(Mg,Fe)SiO_3$-pPv and numerical modeling of convection using polycrystal plasticity to predict strain and anisotropy in D″.

We deformed a sample of polycrystalline $(Mg_{0.9},Fe_{0.1})SiO_3$-pPv plastically in the diamond anvil cell in compression between 145 and 157 GPa and observed the evolution of LPO in situ using angle dispersive radial x-ray diffraction (fig. S1) at the High-Pressure Collaborative Access Team (HPCAT) of the Advanced Photon Source (beamline 16-ID-B). Starting material was a powder of natural orthopyroxene (*14*) mixed with 10 weight percent Pt powder that served as a laser absorber. The sample was initially compressed to high pressure, at which we could not observe coherent diffraction from within the sample, and then converted into the pPv phase by laser heating at different sample positions at a temperature of 1700 K for 20 min and 2000 K for ~15 min. After the phase transformation, pressure and differential stress in the sample were 145 and 7.2 GPa, respectively. They were then increased in two steps to 157 and 8.5 GPa over the course of 30 hours. At every step, we collected radial diffraction patterns to evaluate the pressure, stress, and LPO in the sample (*14*) (table S1).

The diffraction images show substantial variations of diffraction peak positions and intensities with orientation relative to the compression direction that can be used to estimate stress and deduce LPO (*14*) (Fig. 1). For instance, we observed that the diffraction intensity in the compression direction is minimal for 004 and 022, whereas it is maximal for 113 and 132. The texture we obtain (*14*) is represented in Fig. 2. In contrast with low-temperature and lower-pressure observations on the Mn_2O_3 (*15*) and $CaIrO_3$ (*16*) pPv analogs, we observed LPO compatible with previous observations on a $MgGeO_3$-pPv analog deformed under similar conditions (*17*) with a clear minimum at (010) and (001). Those LPO are formed immediately upon synthesizing and heating $(Mg,Fe)SiO_3$-pPv at high pressure. Minima observed at (010) and (001) preclude slip on (001) and (010) planes, and a comparison of observed textures and results from viscoplastic self-consistent (VPSC) polycrystal plasticity simulations (*18*) indicate that the deformation is likely dominated by slip on planes such as (100) or (110), in agreement with results of first-principles modeling of stacking fault energetics and shear elastic constants SiO_3 (*19*) but in disagreement with first-principles modeling of dislocation cores based on the Peierls model that suggest [001](010) as the easiest slip system (*20*).

There are limitations in our experiment: time scale, grain size, strain, temperature, and deviatoric stresses are quite different from those in D″. Moreover, LPOs are formed immediately upon synthesizing and heating the pPv phase and do not evolve greatly upon further compression. However, assuming that (100) and (110) slip also applies to $(Mg,Fe)SiO_3$-pPv under deep mantle conditions, we simulated the development of LPO in $(Mg,Fe)SiO_3$-pPv in D″ combining geodynamic information about macroscopic deformation and the microscopic deformation mechanisms found in the experiment (table S2). Deformation in D″ can be quite complex because it is coupled to larger-scale mantle-wide convective processes. Therefore, we performed our modeling using the entire mantle domain. We used the numerical convection code Citcom (*21*) with the addition of Lagrangian tracers to obtain a proper estimation of the deformational characteristics of

[1]Department of Earth and Planetary Science, University of California, Berkeley, CA 94720, USA. [2]Laboratoire de Structure et Propriétés de l'Etat Solide, UMR CNRS 8008, Université des Sciences et Technologies de Lille, 59655 Villeneuve d'Ascq, France. [3]School of Earth and Space Exploration, Arizona State University, Box 871404, Tempe, AZ 85287–1404, USA. [4]Department of Geosciences, Princeton University, Princeton, NJ 08544, USA. [5]High-Pressure Collaborative Access Team, Carnegie Institution of Washington, Argonne, IL 60439, USA.

*To whom correspondence should be addressed. E-mail: sebastien.merkel@univ-lille1.fr
†Present address: Consortium for Advanced Radiation Sources, University of Chicago, Argonne, IL 60439, USA.
‡Present address: GeoForschungsZentrum Potsdam, Division 4.1, Telegrafenberg, 9-14482 Potsdam, Germany.

mantle strain expected in D″ and tracked deformation in tracers along several streamlines by computing the left-stretch tensor at each step (*14*, *22*, *23*). The two-dimensional (2D) convection calculation employed a Rayleigh number of 10^7, stress-free boundaries, a temperature-dependent rheology, and a viscosity jump of a factor of 50 across the 660-km phase transition (*14*). The formation of a rigid lid was inhibited by imposing a maximum allowable viscosity for the uppermost portion of the model, allowing strong slabs to form. As is typical for geodynamical modeling, we employed the Boussinesq approximation to minimize the number of free parameters. This approximation excludes the effects of compressibility, viscous dissipation, adiabatic heating/cooling, and buoyancy effects due to phase transitions, including the Pv-pPv phase transition. We would expect that our predicted strain values would be slightly modified with the inclusion of these smaller-order physical processes; however, given the uncertainties in the model parameters, we predict that the difference would be minor, particularly for this study.

We began tracking deformation in slab regions at about 290 km above the CMB, corresponding to an approximate depth at which the Pv-to-pPv phase transition is expected to occur. The general trend of strain appears to be similar for most tracers and is characterized by horizontal stretching as slab material impinges upon the CMB (Fig. S4). After investigating several streamlines and observing similar trends, we concentrated on one particular streamline for use in polycrystal plasticity models (*18*). Accumulated strains along a streamline are very large and, assuming that all this strain is accommodated by dislocation glide, polycrystal plasticity simulations would predict very sharp textures, close to a single crystal. This is clearly not realistic. At high temperatures, strain may be partially accommodated by climb, boundary diffusion, and dynamic recrystallization that may significantly weaken texture development. Furthermore, secondary phases may be present. Thus, after several tests (*14*), we found that a reasonable assumption is that 10% of the plastic strain recorded by the tracer is accommodated by dislocation glide in pPv and the rest by mechanisms that do not produce preferred orientation. Using the VPSC model, we simulated the LPO evolution of an aggregate of 2000 grains at each time step of the convection model. Most of the strain (Fig. 3 and fig. S5) occurs as the aggregate reaches the CMB and flows parallel to it. This configuration is very similar to a combination of pure and simple shear parallel along the freeslip surface of the CMB. As the tracer descends into D″, we observe very little development of LPO (Fig. 3A). Texture develops rapidly between steps 1000 (Fig. 3A) and 2000 (Fig. 3B) as the tracer turns at the CMB. The texture strengthens and evolves only moderately as the particle moves along the CMB (up to step 5000) (Fig. 3C) and is later modified during upwelling (Fig. 3D).

We obtained an estimate of expected anisotropies in the D″ by averaging the single-crystal elastic tensors as a function of crystallographic orientation. From the aggregate elastic tensor, we then calculated seismic velocities in different directions. First-principles calculations provide single-crystal elastic moduli for $MgSiO_3$-pPv at high pressure and high temperature (*24*, *25*) (table S3).

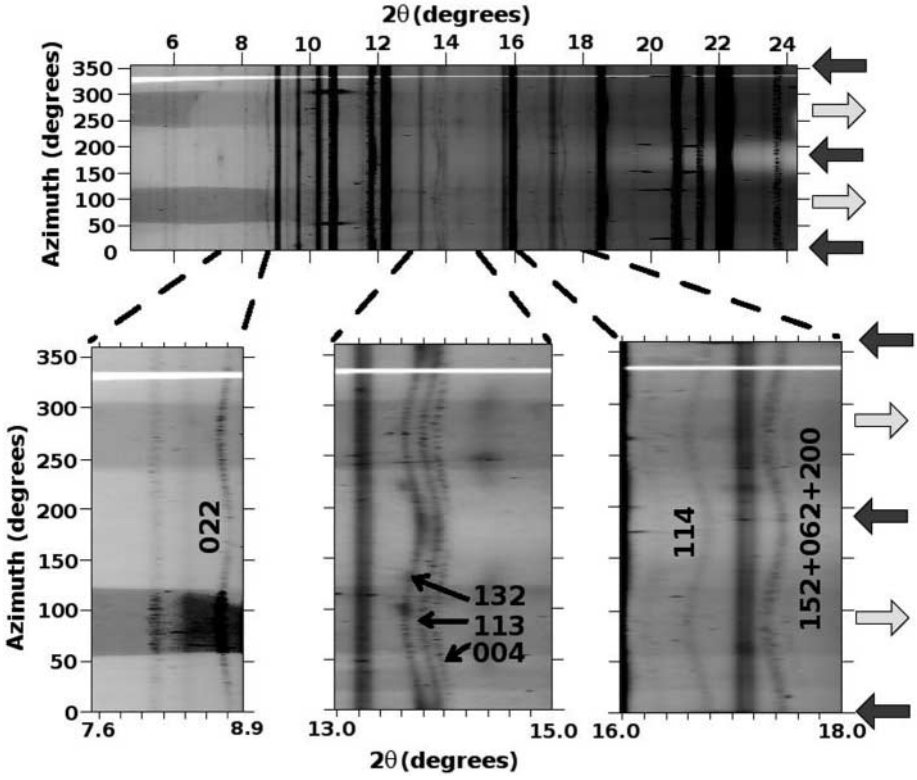

Fig. 1. Unrolled diffraction image of $(Mg,Fe)SiO_3$-pPv measured in radial diffraction, in situ, at 145 GPa. The directions of maximum and minimum stress are indicated by the black and gray arrows on the right, respectively. LPO and differential stress are deduced from the variations of diffraction intensity and peak position with orientation. Miller indices of the diffraction lines from the $(Mg,Fe)SiO_3$-pPv sample actually used in the analysis are labeled on the figure. Diffraction lines with no evidence of stress (straight lines) are from the gasket.

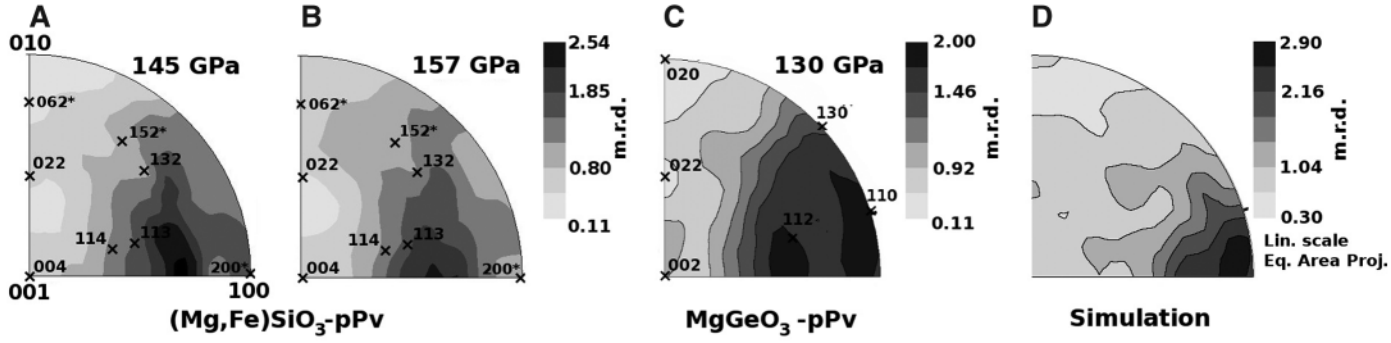

Fig. 2. Inverse pole figure showing the preferred orientation pattern in $(Mg,Fe)SiO_3$-pPv in compression measured (**A**) at 145 GPa just after converting the material to the pPv phase, (**B**) at 157 GPa, (**C**) in $MgGeO_3$ pPv at 130 GPa (*17*), and (**D**) simulated after 20% compressive strain with models that favor slip on (100) and (110). Equal-area projection is used, and linear contours express pole densities in multiples of a random distribution. Reflections used for inverting the orientation distribution function are indicated in the experimental inverse pole figures. The 152, 062, and 200 peaks of $(Mg,Fe)SiO_3$-pPv overlap and are not well resolved.

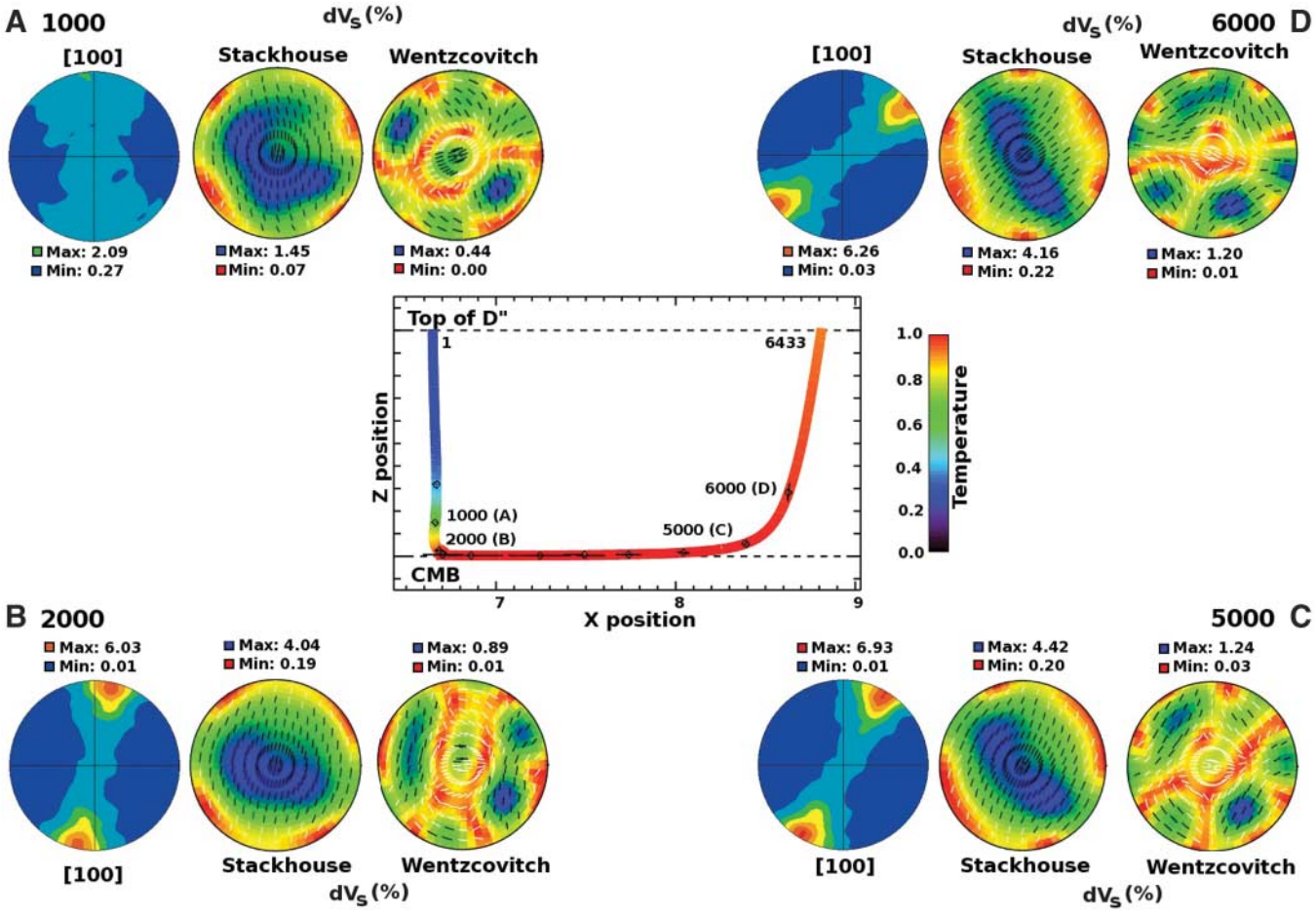

Fig. 3. Modeled temperature, strain, texture, and shear wave splitting from silicate post-perovskite in D″. The central figure illustrates the evolution of temperature and strain along a streamline. Temperatures are normalized so that $T = 0$ at Earth's surface and $T = 1$ at the CMB, strains are indicated by the black lines representing the evolution of maximum and minimum stretch of the Lagrangian particle for every 500 time steps, and numbers are time-step numbers. Panels (**A**) to (**D**) present the modeled 3D [100] orientations, shear wave splitting dV_S, and fastest shear wave polarizations at time steps 1000, 2000, 5000, and 6000, respectively. Shear wave splitting was calculated using the elastic moduli of Stackhouse *et al*. (*24*) and Wentzcovitch *et al*. (*25*). Linear scale, equal area projection. Contours for the [100] and dV_S pole figures are expressed in multiples of a random distribution and percentage, respectively. Black and white lines (for low and high anisotropies, respectively) indicate the direction of polarization of the fast shear wave.

The results of the two calculations differ significantly, and we decided to include both in our analysis (figs. S8 to S10). As the tracer plunges into the D″ layer, we observe very little anisotropy. It develops rapidly between steps 1000 and 2000 (Fig. 3, A and B), as the tracer reaches the CMB. At step 5000 (Fig. 3C), before entering the upwelling, shear wave splitting reaches 4.42% and 1.24% with the elastic moduli of Stackhouse *et al*. (*24*) and Wentzcovitch *et al*. (*25*), respectively.

Most seismic observations of shear wave polarization anisotropy in D″ involve delays of vertically polarized *S* wave components (*SV*) relative to horizontally polarized *S* wave components (*SH*) for paths that graze horizontally through the D″ region (*26*). However, other studies show tilted transverse anisotropy (*27*, *28*) or local variations of fast polarization directions (*29*–*31*). Our predictions of shear wave polarization anisotropies depend strongly on the choice of elastic moduli. Using both models, we found a significant depth dependence of the anisotropy that only develops near and beyond the turning point of a downwelling slab (Fig. 3 and figs. S8 to S10). In a slablike environment, we also found that the anisotropy for waves propagating parallel to the CMB should produce loosely symmetric patterns. Using the elastic moduli of Stackhouse *et al*. (*24*), we predict a maximum anisotropy of 4% perpendicular to the direction of flow, with the direction of fast polarization ranging from 60° to 90° ($V_{SH} < V_{SV}$). Using the elastic moduli of Wentzcovitch *et al*. (*25*), we obtain lower values of anisotropy with dV_S ranging between 0.5 and 0.6%, with a fast polarization near 0° ($V_{SH} > V_{SV}$) for waves traveling perpendicular to the direction of flow. Waves traveling parallel to the direction of flow would show varying anisotropies with very little anisotropy near the downwelling and up to 1.2% before upwelling, again with a fast polarization near 0° ($V_{SH} > V_{SV}$).

Predictions using the elastic moduli of Stackhouse *et al*. (*24*) systematically imply $V_{SH} < V_{SV}$ and are inconsistent with most seismic measurements that find either $V_{SH} > V_{SV}$ or locally varying fast polarization directions. Using the elastic moduli of Wentzcovitch *et al*. (*25*), we obtain complex patterns of anisotropies with lower amplitude than observed seismically. Although many characteristics of D″ are consistent with the properties of post-perovskite, other phases or structural mechanisms (e.g., layering) may be necessary to explain the seismic anisotropy of the region. Our study shows how ultrahigh pressure experiments on silicate post-perovskites combined with microscale (plasticity) and macroscale (mantle flow) modeling provide the means to test our understanding of deformation behavior at the base of Earth's mantle.

References and Notes

1. T. Lay, Q. Williams, E. J. Garnero, *Nature* **392**, 461 (1998).
2. R. D. van der Hilst *et al.*, *Science* **315**, 1813 (2007).
3. M. Panning, B. Romanowicz, *Science* **303**, 351 (2004).
4. A. K. McNamara, P. E. van Keken, S. I. Karato, *Nature* **416**, 310 (2002).
5. Q. Williams, E. J. Garnero, *Science* **273**, 1528 (1996).
6. J. M. Kendall, in *The Core-Mantle Boundary Region*, M. Gurnis, M. E. Wysession, E. Knittle, B. A. Buffet, Eds.

(American Geophysical Union, Washington, DC, 1998), pp. 97–118.
7. M. Murakami, K. Hirose, K. Kawamura, N. Sata, Y. Ohishi, *Science* **304**, 855 (2004).
8. A. R. Oganov, S. Ono, *Nature* **430**, 445 (2004).
9. D. Helmberger, T. Lay, S. Ni, M. Gurnis, *Proc. Nat. Acad. Sci. U.S.A.* **102**, 17257 (2005).
10. J. Wookey, S. Stackhouse, J. Kendall, J. Brodholt, G. D. Price, *Nature* **438**, 1004 (2005).
11. K. Hirose, *Rev. Geophys.* **44**, RG3001 (2006).
12. W. L. Mao *et al.*, *Science* **312**, 564 (2006).
13. T. Lay, J. Hernlund, E. J. Garnero, M. S. Thorne, *Science* **314**, 1272 (2006).
14. Materials and methods are available as supporting material on *Science* Online.
15. J. Santillán, S. Shim, G. Shen, V. Prakapenka, *Geophys. Res. Lett.* **33**, L15307 (2006).
16. D. Yamazaki, T. Yoshino, H. Ohfuji, J. Ando, A. Yoneda, *Earth Planet. Sci. Lett.* **252**, 372 (2006).
17. S. Merkel *et al.*, *Science* **311**, 644 (2006).
18. R. A. Lebensohn, C. N. Tomé, *Acta Metal. Mater.* **41**, 2611 (1993).
19. A. R. Oganov, R. Martonák, A. Laio, P. Raiteri, M. Parrinello, *Nature* **438**, 1142 (2005).
20. P. Carrez, D. Ferré, P. Cordier, *Nature* **446**, 68 (2007).
21. L. Moresi, M. Gurnis, *Earth Planet. Sci. Lett.* **138**, 15 (1996).
22. A. K. McNamara, P. E. van Keken, S.-I. Karato, *J. Geophys. Res.* **108**, 2230 (2003).
23. A. K. McNamara, S. Zhong, *Earth Planet. Sci. Lett.* **222**, 485 (2004).
24. S. Stackhouse, J. P. Brodholt, J. Wookey, J.-M. Kendall, G. D. Price, *Earth Planet. Sci. Lett.* **230**, 1 (2005).
25. R. Wentzcovitch, T. Tsuchiya, J. Tsuchiya, *Proc. Nat. Acad. Sci. U.S.A.* **103**, 543 (2006).
26. M. Moore, E. J. Garnero, T. Lay, Q. Williams, *J. Geophys. Res.* **109**, B02319 (2004).
27. E. J. Garnero, V. Maupin, T. Lay, M. J. Fouch, *Science* **306**, 259 (2004).
28. J. Wookey, J. M. Kendall, G. Rümpker, *Geophys. J. Int.* **161**, 829 (2005).
29. S. A. Russell, T. Lay, E. J. Garnero, *Nature* **396**, 255 (1998).
30. S. A. Russell, T. Lay, E. J. Garnero, *J. Geophys. Res.* **104**, 13,183 (1999).
31. J. M. Rokosky, T. Lay, E. J. Garnero, *Earth Planet. Sci. Lett.* **248**, 411 (2006).

32. We thank D. Mainprice for his petrophysics software package, P. Liermann for assistance during the experiment, and the two anonymous reviewers for their comments. This work was supported by NSF grants EAR-0510383 and EAR-0456356 (T.S.D., H.R.W., and A.K.M.) and the Carnegie/Department of Energy Alliance Center (T.S.D. and H.R.W.). Experiments were performed at HPCAT (Sector 16), Advanced Photon Source (APS), Argonne National Laboratory. Use of the HPCAT facility was supported by Department of Energy (DOE) Basic Energy Sciences (BES), DOE National Nuclear Security Administration, NSF, Department of Defense (DOD) Tank-Automotive and Armaments Command, and the W. M. Keck Foundation. Use of the APS was supported by DOE-BES under contract W-31-109-ENG-38. S.M. and S.S. also acknowledge support from the Miller Institute for Basic Research in Science.

Supporting Online Material

www.sciencemag.org/cgi/content/full/316/5832/1729/DC1
Materials and Methods
Figs. S1 to S10
Tables S1 to S3
References

31 January 2007; accepted 13 April 2007
10.1126/science.1140609

Weak Northern and Strong Tropical Land Carbon Uptake from Vertical Profiles of Atmospheric CO_2

Britton B. Stephens,[1]* Kevin R. Gurney,[2] Pieter P. Tans,[3] Colm Sweeney,[3] Wouter Peters,[3] Lori Bruhwiler,[3] Philippe Ciais,[4] Michel Ramonet,[4] Philippe Bousquet,[4] Takakiyo Nakazawa,[5] Shuji Aoki,[5] Toshinobu Machida,[6] Gen Inoue,[7] Nikolay Vinnichenko,[8]† Jon Lloyd,[9] Armin Jordan,[10] Martin Heimann,[10] Olga Shibistova,[11] Ray L. Langenfelds,[12] L. Paul Steele,[12] Roger J. Francey,[12] A. Scott Denning[13]

Measurements of midday vertical atmospheric CO_2 distributions reveal annual-mean vertical CO_2 gradients that are inconsistent with atmospheric models that estimate a large transfer of terrestrial carbon from tropical to northern latitudes. The three models that most closely reproduce the observed annual-mean vertical CO_2 gradients estimate weaker northern uptake of −1.5 petagrams of carbon per year (Pg C year^{-1}) and weaker tropical emission of +0.1 Pg C year^{-1} compared with previous consensus estimates of −2.4 and +1.8 Pg C year^{-1}, respectively. This suggests that northern terrestrial uptake of industrial CO_2 emissions plays a smaller role than previously thought and that, after subtracting land-use emissions, tropical ecosystems may currently be strong sinks for CO_2.

Our ability to diagnose the fate of anthropogenic carbon emissions depends critically on interpreting spatial and temporal gradients of atmospheric CO_2 concentrations (*1*). Studies using global atmospheric transport models to infer surface fluxes from boundary-layer CO_2 concentration observations have generally estimated the northern mid-latitudes to be a sink of approximately 2 to 3.5 Pg C year^{-1} (*2*–*5*). Analyses of surface ocean partial pressure of CO_2 (*2*), atmospheric carbon isotope (*6*), and atmospheric oxygen (*7*) measurements have further indicated that most of this northern sink must reside on land. Tropical fluxes are not well constrained by the atmospheric observing network, but global mass-balance requirements have led to estimates of strong (1 to 2 Pg C year^{-1}) tropical carbon sources (*4*, *5*). Attribution of the Northern Hemisphere terrestrial carbon sink (*8*–*13*) and reconciliation of estimates of land-use carbon emissions and intact forest carbon uptake in the tropics (*14*–*19*) have motivated considerable research, but these fluxes remain quantitatively uncertain. The full range of results in a recent inverse model comparison study (*5*), and in independent studies (*3*, *20*, *21*), spans budgets with northern terrestrial uptake of 0.5 to 4 Pg C year^{-1}, and tropical terrestrial emissions of −1 to +4 Pg C year^{-1}. Here, we analyzed observations of the vertical distribution of CO_2 in the atmosphere that provide new constraints on the latitudinal distribution of carbon fluxes.

Previous inverse studies have used boundary-layer data almost exclusively. Flask samples from profiling aircraft have been collected and measured at a number of locations for up to several decades (*22*–*24*), but efforts to compile these observations from multiple institutions and to compare them with predictions of global models have been limited. Figure 1 shows average vertical profiles of atmospheric CO_2 derived from flask samples collected from aircraft during midday at 12 global locations (fig. S1), with records extending over periods from 4 to 27 years (table S1 and fig. S2) (*25*). These seasonal and annual-mean profiles reflect the combined influences of surface fluxes and atmospheric mixing. During the summer in the Northern Hemisphere, midday atmospheric CO_2 concentrations are generally lower near the surface than in the free troposphere, reflecting the greater impact of terrestrial photosynthesis over industrial emissions at this time. Sampling locations over or immediately downwind of continents show larger gradients than those over or downwind of ocean basins in response to stronger land-based fluxes, and higher-latitude locations show greater CO_2 drawdown at high altitude. Conversely, during the winter, respiration and fossil-fuel sources lead to elevated low-altitude atmospheric CO_2 concentrations at northern locations. The gradients are comparable in magnitude in both seasons, but the positive

[1]National Center for Atmospheric Research, Boulder, CO 80305, USA. [2]Department of Earth and Atmospheric Sciences, Purdue University, West Lafayette, IN 47907, USA. [3]National Oceanic and Atmospheric Administration, Boulder, CO 80305, USA. [4]Le Laboratoire des Sciences du Climat et l'Environnement, 91191 Gif sur Yvette, France. [5]Center for Atmospheric and Oceanic Studies, Tohoku University, Sendai 980-8578, Japan. [6]National Institute for Environmental Studies, Onogawa, Tsukuba 305-8506, Japan. [7]Graduate School of Environmental Studies, Nagoya University, Nagoya City 464-8601, Japan. [8]Central Aerological Observatory, Dolgoprudny, 141700, Russia. [9]School of Geography, University of Leeds, West Yorkshire, LS2 9JT, UK. [10]Max Planck Institute for Biogeochemistry, 07701 Jena, Germany. [11]Sukachev Institute of Forest, Krasnoyarsk, 660036, Russia. [12]Commonwealth Scientific and Industrial Research Organisation (CSIRO) Marine and Atmospheric Research, Aspendale, Victoria 3195, Australia. [13]Department of Atmospheric Science, Colorado State University, Fort Collins, CO 80523, USA.

*To whom correspondence should be addressed. E-mail: stephens@ucar.edu
†Deceased.